Catalysis Science & Technology

Accepted Manuscript

ROYAL SOCIETY OF CHEMISTRY

www.rsc.org/catalysis

Catalysis Science & Technology

ARTICLE

Received 00th January 20xx,

Accepted 00th January 20xx

DOI: 10.1039/x0xx00000x

www.rsc.org/

Preparation and Characterization of PtIr Alloy Dendritic Nanostructures for Superior Electrochemical Activity and Stability in Oxygen Reduction and Ethanol Oxidation Reactions

Young-Woo Lee,‡[a,b] Eui-Tak Hwang,‡[a] Da-Hee Kwak[a] and Kyung-Won Park*[a]

Dendritic Pt-based alloy nanostructures have been known to exhibit improved electrocatalytic properties due to their particularly modulated surface and electronic structures favorable for alcohol oxidation and oxygen reduction reactions. We prepare the PtIr alloy nanoparticles NPs with a dendritic shape as a three-dimensional structure for enhanced ethanol oxidation reaction (EOR) and oxygen reduction reaction (ORR) by thermal-decomposition in the presence of cetyltrimethyl-ammonium chloride (CTAC) as a surfactant agent. The PtIr alloy dendritic nanostructures show a well-defined alloy nanostructure with three-dimensional structures analyzed using TEM, XPS, and XRD. In particular, the PtIr alloy nanostructures exhibit 2.74 times higher electrochemical active surface areas (EASAs) than commercial Pt/C. Also, in EOR, the PtIr alloy dendritic electrocatalyst indicates excellent electrochemical properties, including high I_f/I_b ratio and current density, great negative on-set potential, and good electrochemical stability compared to commercial Pt/C electrocatalyst. In addition, the PtIr alloy dendritic electrocatalyst exhibits enhanced electrochemical activity and stability i.e., 3.19 times higher specific mass-kinetic activity than commercial Pt/C electrocatalyst, and a reduction of 8 mV of half-wave potential in ORR. The improved electrochemical activity and stability of the PtIr alloy dendritic electrocatalyst in EOR and ORR are ascribed to dendritic structures, the surface state of the electrocatalyst, and the controlled electronic structure due to the Ir atoms in the alloy phase.

Introduction

Metallic platinum (Pt) is well known as the most effective electrocatalyst for fuel oxidation and oxygen reduction reactions in low-temperature fuel cells.[1-3] Despite its electrochemical activity for oxidation and reduction in fuel cells, polycrystalline Pt electrocatalyst has exhibited critical problems such as high cost and low specific electrocatalytic activity.[4-8] In particular, due to the enhanced electrocatalytic activity and reduced cost, the surface modification, alloy formation, and core-shell structure in the Pt-based electrocatalysts have been intensively studied.[9-13] Among these studies, the alloy nanostructures could show much improved specific electrocatalytic activity in fuel oxidation and oxygen reduction reaction compared to pure Pt electrocatalyst by alloying 2nd metallic elements such as Pd[14,15], Ir[16,17], Sn[18], Ru[19], Fe[20], and Co.[21] In the case of fuel oxidation reactions, Pt-based alloy electrocatalysts have exhibited an enhanced activity due to a dual-functional effect and downshift of the d-band center of the pure Pt electronic structure resulting in a reduced generation rate of intermediate species during the reactions.[22,23] Furthermore, an enhanced electrocatalytic activity of Pt-based alloy electrocatalysts for oxygen reduction reaction may be attributed to the modified electronic and surface structures with 2nd metallic materials in Pt structures.[24,25]

Of the 2nd metallic elements, iridium (Ir) has been well known as an effective subcatalyst in Pt-based alloy electrocatalysts for ethanol oxidation and oxygen reduction reactions in acidic electrolytes. In the case of EOR, Ir has exhibited excellent electrochemical properties (i.e., facile breaking of C-C bond and CO-tolerance effect), based on electrochemical analysis and density functional theory calculations.[26,27] Furthermore, an improved electrocatalytic activity of PtIr alloy electrocatalysts for ORR due to the geometric factor has been intensively studied by alloying the degree between Pt and Ir atoms and coverage of OH on the Ir surface at a greater negative potential than that of Pt surface.[27,28] In contrast, the spherical PtIr NPs have an enhanced initial electrochemical activity for both EOR and ORR; however, low electrochemical stability is observed due to the serious aggregation of NPs during the electrochemical reactions. In particular, zero- to three-dimensional Pt-based nanostructures with controlled surface structures for EOR and ORR have been developed to improve the electrochemical

[a] Department of Chemical Engineering, Soongsil University, Seoul 156743, Republic of Korea. E-mail: kwpark@ssu.ac.kr
[b] Department of Engineering Science, University of Oxford, Oxford OX1 3PJ, United Kingdom.
‡ Both of these authors contributed equally to this work.
† Electronic supplementary information (ESI) available: Figure S1-S8 contains TEM, EDX, and electrochemical data. See DOI: 10.1039/x0xx00000x

properties of the electrocatalysts due to favorable facets such as low-index or high-index.[29-36] Furthermore, among Pt-based nanostructures, dendritic and flower-like nanostructures with three-dimensional structure for electrochemical power sources have shown much enhanced electrocatalytic activity and stability due to high surface area of dendritic structures and favorable exposed facets.[37,38] Thus, three-dimensional PtIr alloy nanostructures with dendritic, star, and flower-like shapes have been proposed to improve electrochemical properties; i.e., enhanced specific activity and stability for EOR and ORR.

Herein, we synthesized the PtIr alloy dendritic NPs with three-dimensional structures for enhanced EOR and ORR using a thermal-decomposition in the presence of CTAC. The morphology and structure of the as-prepared NPs were characterized using field emission transmission electron microscopy (FE-TEM) and X-ray diffraction (XRD). The chemical states and elemental compositions of the as-prepared NPs were characterized using X-ray photoelectron spectroscopy (XPS), energy dispersive X-ray spectroscopy (EDX), and inductively coupled plasma mass spectrometry (ICP-MS). The electrochemical and electrocatalytic properties of the as-prepared electrocatalysts in EOR and ORR were obtained using a typical electrochemical cell with a potentiostat.

Experimental Section

Synthesis of the PtIr alloy dendritic nanostructures

The PtIr alloy dendritic NPs were prepared by reducing Pt and Ir salt in an organic-based solution in the presence of CTAC as a surfactant agent. All chemicals used were of analytical grade. The solution containing 5 mL 1-octadecene (90%, Aldrich) and 4 mL oleylamine (70%, Aldrich) with 4.5 mM $Pt(acac)_2$ (97%, Aldrich) and 1.5 mM $IrCl_3 \cdot H_2O$ (99.9%, Aldrich) was prepared in a 30 mL vial. The metal salt solution was kept at 70 ^{o}C for 30 min with continuous stirring. The solution containing 10 mL 1-octadecene (90%, Aldrich), 2 mL oleylamine (70%, Aldrich), 2 mL oleic acid (65~88%, Aldrich), and 2 mL CTAC (25%, Aldrich) was prepared in a three neck flask (50 mL) under a nitrogen atmosphere. The mixed solution was kept for 30 min at 250 ^{o}C. The previously prepared metal salt solution was injected into the mixed solution with continuous stirring and kept for 3 h at 250 ^{o}C until the metal salts were completely reduced under nitrogen atmosphere. The resulting black colloid solution was rapidly cooled by placing the product into hexane.

Preparation of carbon-supported PtIr alloy electrocatalyst

For acid treatment of carbon black, Vulcan XC-72R as a carbon support was kept in the mixed sulfuric/nitric acids at 80 ^{o}C for 12 h under vigorous stirring and then washed with water and ethanol several times to remove impurities. The as-prepared PtIr alloy NPs were dispersed in the deionized water containing dispersed carbon powder and then, (40 wt%) deposited on the as-treated carbon black after the addition of 5 ml 0.5 M H_2SO_4 (95%, SAMCHUN). To completely remove the remaining impurities, the product was maintained in a 30 ml acetic acid solution (99.7%, SAMCHUN) at 80 ^{o}C for 12 h. The resulting precipitate was washed with acetone, ethanol, and water to remove impurities and dried in an oven at 50 ^{o}C.

Preparation of carbon supported spherical PtIr alloy electrocatalyst

The spherical PtIr alloy (40 wt%) deposited on carbon black was prepared by simultaneously reducing Pt and Ir salts using a $NaBH_4$ reduction method. For smaller size and good dispersion of PtIr NPs on carbon black, we used poly (vinyl pyrrolidone) (PVP, Mw 29,000, Aldrich) as a surfactant agent. The carbon black powder was homogeneously dispersed in deionized water and then $H_2PtCl_6 \cdot xH_2O$ (99.995%, Aldrich), $IrCl_3 \cdot xH_2O$ (99.9%, Aldrich), and PVP were dissolved in the solution with continuous stirring for 30 min. After 30 min, NaBH4 solution as a reductant with an excess amount was added to the metal salt solution with continuous stirring at 25 ^{o}C for 2 h. Finally, the resulting precipitate was several times washed with acetone, ethanol, and deionized water and then dried in an oven at 50 ^{o}C.

Structural and chemical analysis

The morphology and size distribution of the electrocatalysts were characterized using an FE-TEM (Tecnai G2 F30 system) operating at 300 kV. TEM samples were prepared by placing drops of electrocatalyst suspension dispersed in ethanol on a carbon coated copper grid. EDX analysis of the electrocatalysts was performed on an FE-TEM (Tecnai G2 F30 system). For the structure analysis of the electrocatalysts, XRD analysis was carried out using a Rigaku X-ray diffractometer with Cu Kα (λ = 0.15418 nm) source with a Ni filter. The source was operated at 40 kV and 100 mA. The 2θ angular scan from 20° to 80° was explored at a scan rate of 3° min-1. For all the XRD measurements, the resolution in the scans was kept at 0.02°. XPS (Thermo Scientific, K-Alpha) analysis was carried out with the Al Kα X-ray source of 1486.8 eV at the chamber pressure below 1 x 10^{-8} Torr and 200 W beam power. All high resolution spectra were collected using a pass energy of 46.95 eV. The step size and time per step were chosen to be 0.025 eV and 100 ms, respectively. Both ends of the baseline were set sufficiently far to avoid distorting the shape of the spectra, including the tails. A small variation of the range of the base line did not affect the relative amount of fitted species (less than 1%). The C 1s electron binding energy was referenced at 284.6 eV and a nonlinear least squares curve fitting program was employed with a Gaussian-Lorentzian production function. Also, the elemental compositions of Pt and Ir in the as-prepared electrocatalysts were measured using an inductively coupled plasma mass spectrometry (ICP-MS, Optima-4300 DV, 45 PerkinElmer).

Electrochemical analysis

The electrochemical properties of the as-prepared electrocatalysts in EOR and ORR were measured in a three-electrode cell at 25 ^{o}C using a potentiostat (Eco Chemie,

AUTOLAB). The electrocatalyst inks were prepared by mixing the electrocatalyst (10 mg), de-ionized water (150 μL), isopropyl alcohol (500 μL), and 5 wt% Nafion solution (58 μL). The glassy carbon working electrode was coated with 0.5 μL of the electrocatalyst inks and dried in a 50 ^{o}C oven. The total metal loading of the electrocatalyst in all the samples was 40 $\mu g\ cm^{-2}_{metal}$. In addition, Pt wire and Ag/AgCl (in saturated 3 M KCl) were used as counter and reference electrodes, respectively. Cyclic voltammograms (CVs) of the electrocatalysts were obtained in Ar-saturated 0.1 M $HClO_4$ and 0.1 M $HClO_4$ + 0.2 M C_2H_5OH with a scan rate of 50 mV s^{-1} at 25 ^{o}C. The CO-stripping voltammetry was measured using CO-saturated 0.1 M $HClO_4$ solution. To evaluate the electrocatalytic stability, the electrocatalysts were kept at 0.5 V (vs. Ag/AgCl) for 7200 s in 0.1 M $HClO_4$ + 0.2 M C_2H_5OH and CVs were then obtained in 0.1 M $HClO_4$ + 0.2 M C_2H_5OH after the stability test. The oxygen reduction current–potential curves were obtained using linear sweep voltammograms (LSVs) at various rotation speeds at 1600 rpm in O_2-saturated 0.1 M $HClO_4$ solution by sweeping the potential from 0.8 to 0 V (vs. Ag/AgCl) at a scan rate of 5 mV s^{-1}. The stability test in ORR was carried out by applying linear potential sweeps for 2000 cycles between 0.4 and 0.9 V (vs. Ag/AgCl) with a scan rate of 50 mV s^{-1} in O_2-saturated 0.1 M $HClO_4$ solution at 25 ^{o}C. The oxygen reduction current-potential curves after the stability test of the electrocatalysts were obtained by sweeping the potential from 0.8 to 0 V (vs. Ag/AgCl) at a scan rate of 5 mV s^{-1} and rotation disk speed of 1600 rpm. All potentials were calibrated with respect to the reversible hydrogen electrode (RHE).[39,40]

Results and Discussion

For EOR and ORR electrocatalysts, we synthesized the PtIr alloy nanostructures by reducing Pt and Ir salts in the presence of CTAC as a surfactant agent in an organic solvent using a thermal decomposition method. The average size and yield of the as-synthesized PtIr NPs are ~58.2 nm and over 99 %, respectively (Fig. 1a and Fig. S1b). As shown in the high-resolution TEM (HR-TEM) image of Figure 1b, the PtIr NP exhibited a three-dimensional dendritic structure, which has a polycrystalline structure indicated by the fast Fourier transform (FFT) patterns in Fig. S1a. The monodispersed size distribution with a high yield of the PtIr NPs results from the presence of CTAC as a surfactant agent in the synthesis. On the other hand, the PtIr NPs synthesized in the absence of CTAC show a poly-dispersed size distribution and irregular shape without a homogeneous assembly between PtIr NPs (Fig. S2). Thus, it is likely that, in the case of the present synthetic approach, CTAC as a surfactant could prevent aggregation among the dendritic-like PtIr NPs, forming pores via the induced inverse micelle structures. Recently, it was reported that metallic nanostructures synthesized using a secondary added surfactant agent such as PVP and hexadecylpyridinium chloride monohydrate in organic solution exhibit a uniform size and shape with a homogeneous distribution without any aggregation.[41,42] Similarly, in our synthetic process in the presence of CTAC, the uniform dendritic shape of PtIr NPs may be attributed to the induced inverse micelle structures and formed spherical void by the self-assembly of CTAC in the thermal decomposition method (Fig. S3). To confirm an elemental distribution in the PtIr NPs, the line scanning profiles of a single NP were obtained using EDX analysis (Fig. 1c). The PtIr NP showed a well-defined alloy phase and homogenous atomic distribution of both Pt and Ir in the structure. Furthermore, as shown in Fig. 1d, elemental mapping images of the PtIr dendritic nanostructure were obtained using high-angle annular dark-field scanning TEM EDX (HAADF-STEM-EDX) spectroscopy. It is evident that the PtIr nanostructure contains a homogeneously mixed phase of Pt (yellow) and Ir (red) in the single NP. As confirmed by the EDX spectrum in Fig. 1e, the elemental compositions of Pt and Ir in the PtIr NPs are 87.5 and 12.5 at%, respectively. Also, as confirmed by ICP-MS, the elemental compositions of Pt and Ir in the as-prepared PtIr NPs are 88.3 and 11.7 at%, respectively. According to TEM and EDX analysis, it is expected that the PtIr alloy dendritic NPs could hold the improved electrocatalytic properties in EOR and ORR because of the homogeneous alloy phase and dendritic nanostructure with both a high surface area and electrochemical active sites.

In particular, to characterize the structural and electrochemical properties of the PtIr alloy NPs on the carbon black (denoted as d-PtIr/C, Fig. S4) for the EOR and ORR, we synthesized spherical PtIr alloy nanostructures deposited on carbon black (denoted as s-PtIr/C) using a borohydride reduction method with PVP as an additive agent compared to commercial Pt/C (40 wt%, E-TEK Co.) (denoted as Pt/C). The average particle size of the metal electrocatalysts in the s-PtIr/C and Pt/C is ~4.2 and ~4.3 nm, respectively (Fig. 2). From the EDX analysis, the elemental compositions of Pt and Ir in the as-prepared s-PtIr/C are 89.5 and 10.5 at%, respectively (Fig. S5). In addition, the elemental compositions of Pt and Ir in the s-PtIr/C confirmed by ICP-MS are 87.8 and 12.2 at%, respectively.

Fig. 3a shows XRD patterns of the d-PtIr/C, s-PtIr/C and Pt/C. The XRD pattern of the d-PtIr/C contains diffraction peaks corresponding to (111), (200), and (220) of a typical face-centered cubic crystal structure with a higher diffraction angle shift in comparison with Pt reference data. Furthermore, the average particle and/or grain sizes of the as-prepared catalysts can be estimated from the Debye-Scherrer equation. The grain size of the dendritic structure of the d-PtIr/C is ~4.94 nm. The particle size of s-PtIr/C and Pt/C is ~3.42 and ~3.16 nm, respectively, which is in good agreement with the TEM data in Fig. 2. Assuming a substitutional solid solution between metallic phases, the higher angle shift of the XRD peaks means a well-defined alloy formation between Pt and Ir. Furthermore, based on Vegard's law using the equation of $d_{PtIr} = x \cdot d_{Pt} + (1-x) \cdot d_{Ir}$, the elemental compositions of Pt and Ir atoms in d-PtIr/C and s-PtIr/C are 87.9 and 12.1 at% and 89.3 and 10.7 at%, respectively, which is in good agreement with the EDX analysis.[3,15]

The chemical states and elemental compositions for the d-PtIr/C were obtained by XPS in comparison with s-PtIr/C and Pt/C as shown in Figure 4. The Pt $4f_{7/2}$ and $4f_{5/2}$ peaks typically appear at ~71 and ~74 eV, respectively, with a theoretical area ratio of 4:3. The Pt $4f_{7/2}$ peaks in the as-prepared NPs consist of metallic and oxide states; i.e., the peaks for Pt^0, Pt^{2+}, and Pt^{4+} at ~71.3, ~72.5, and ~74.2 eV, respectively (Figure 4a-c). Interestingly, the chemical phases of Pt in the d-PtIr/C and s-PtIr/C exhibited a higher metallic state ratio than that in s-Pt NPs because the nitrogen atmosphere during our synthesis process can be protected from oxidative etching and surface oxidation reaction of the metallic electrocatalysts. On the other hand, the Ir $4f_{7/2}$ and $4f_{5/2}$ peaks typically appear at ~61 and ~63 eV, respectively, with a theoretical area ratio of 4:3. The Ir 4f peaks consist of metallic and oxide states, i.e., the peaks for Ir^0, Ir^{2+}, and Ir^{4+} at 60.9, 61.9, and 62.8 eV, respectively (Figure 4d and e). In particular, the metallic states of Pt and Ir in the d-PtIr/C exhibited a much higher portion of over 60% compared to Pt/C (40%) (Figure 4f). Furthermore, the elemental compositions of Pt and Ir in the as-prepared PtIr/C electrocatalysts measured using XPS are as follows: 90.2 at% of Pt and 9.8 at% of Ir in the d-PtIr/C, 91.3 at% of Pt and 8.7 at% of Ir in the s-PtIr/C. From the XPS analysis, the d-PtIr/C and s-PtIr/C would be expected to improve electrochemical activity in EOR and ORR in comparison with the Pt NPs due to the high alloying according to a highly metallic state of Pt and Ir.[26-28,43-45] Also, according to Hwang et al. the change of electronic structure among both Pt and Ir in the alloy phase can induce a downshift of the d-band center of the Pt electronic structure, resulting in enhanced electrochemical properties in comparison with pure Pt electrocatalyst.[46] By comparing the EDX, XRD, XPS, and ICP data, it can be concluded that the d-PtIr/C and s-PtIr/C hold a homogeneous distribution of Pt and Ir atoms in both the bulk and surface of the alloy dendritic NPs, as shown in Fig. S6.

To characterize the electrochemical properties of the as-prepared electrocatalysts (d-PtIr/C, s-PtIr/C, and Pt/C) in an acid solution, the CVs of the as-prepared electrocatalysts in Ar-saturated 0.1 M $HClO_4$ were obtained as shown in Fig. 5a. The EASAs of the electrocatalysts were measured by integrating the charges on the H_{upd} adsorption/desorption region.[11,12] The EASA of the d-PtIr/C (71.05 $m^2\ g^{-1}$) was much higher compared to s-PtIr/C (34.67 $m^2\ g^{-1}$) and Pt/C (25.96 $m^2\ g^{-1}$) due to the three-dimensional dendritic nanostructure of the d-PtIr (Fig. 5e). To characterize the electrochemical activity of the as-prepared electrocatalysts for EOR, CVs were obtained in 0.1 M $HClO_4$ + 0.2 M C_2H_5OH, as shown in Fig. 5b-d. The onset potentials of the electrocatalysts in EOR were measured by comparing the CVs in 0.1 M $HClO_4$ with or without 0.2 M C_2H_5OH, as shown in the insets of Fig. 5b-d. In particular, the onset potential of the d-PtIr/C (0.341 V) in EOR is much lower than the s-PtIr/C (0.344 V) and Pt/C (0.353 V), indicating the improved electrocatalytic activity of the d-PtIr/C for EOR. The maximum current densities at the forward scan of the d-PtIr/C, s-PtIr/C, and Pt/C are 13.76, 8.19, and 6.22 mA cm^{-2}, respectively. The improved EOR activity of the d-PtIr/C might result from the three-dimensional dendritic-like nanostructure and the dominant surface metallic phases of Pt and Ir.[6,7] In alcohol electrooxidation reactions, Goodenough et al. suggested the anodic peak in the reverse scan might be attributed to the removal of the incompletely oxidized intermediate species formed in the forward scan.[47] Hence, the ratio of the forward anodic peak current density (I_f) to the reverse anodic peak current density (I_b) (i.e., I_f/I_b), can be used to describe the tolerance of the electrocatalyst to the accumulation of intermediate species during ethanol electrooxidation.[48] The I_f/I_b ratios of the d-PtIr/C (1.55) and s-PtIr/C (1.54) were approximately 1.2 times greater than that of Pt/C. Accordingly, the relatively enhanced electrochemical activity of both PtIr alloy electrocatalysts (d-PtIr/C and s-PtIr/C) implies a more complete ethanol electrooxidation reaction than pure Pt electrocatalyst due to facile breaking of C-C bond in the alloy structure formed by adding Ir. Recently, Hwang et al. reported that Ir in PtIr electrocatalyst could assist in the removal of adsorbed CO species from the Pt surface during alcohol electrooxidation reaction.[46] Besides, to characterize CO-tolerance of the as-prepared electrocatalysts, CO oxidative stripping voltammetry was performed as shown in Fig. S7. The d-PtIr/C and s-PtIr/C electrocatalysts exhibited much lower on-set potential toward CO-oxidation than the Pt/C electrocatalyst. This suggests that the enhanced EOR activity and CO-tolerance of the both PtIr/C electrocatalysts might result from bifunctional effect by Ir into Pt alloying phase. Furthermore, to evaluate the electrocatalytic stability of the electrocatalysts in EOR, a plot of oxidation current versus time (Chronoampero-metry, CA) for the as-prepared electrocatalysts was obtained in 0.1 M $HClO_4$ + 0.2 M C_2H_5OH, as indicated in Fig. S8. The d-PtIr/C maintained a much higher initial and final current density of 0.44 mA cm^{-2} in comparison with s-PtIr/C and Pt/C (0.31 and 0.07 mA cm^{-2}, respectively). After the EOR stability test, in particular, the current density (3.55 mA cm^{-2}) of the d-PtIr/C at 0.65 V in CVs of ethanol oxidation slightly decreased; i.e., the reduction of 24.5% from the initial value (4.70 mA cm^{-2}) (Fig. 5f)). In contrast, the s-PtIr/C and Pt/C supported quite low current densities and thus showed the current reduction of 52.8% and 45.2%, respectively, after the stability test. This implies that the d-PtIr/C exhibited much improved electrocatalytic activity and stability for EOR due to a stable dendritic nanostructure and high EASA compared to s-PtIr/ C and Pt/C.

To characterize the electrochemical properties of the as-prepared electrocatalysts for ORR in acid electrolyte, we measured the ORR electrochemical activity in O_2-saturated $HClO_4$ solution using LSVs at 1600 rpm (Fig. 6a-c). The current density (1.28 mA cm^{-2}) of the d-PtIr/C based on the geometric area of glassy carbon at 0.6 V was much higher than that of s-PtIr/C and Pt/C. Furthermore, Fig. 6d exhibits the specific area-kinetic activity curves (Potential vs. $J_{k,Area}$) of the as-prepared electrocatalysts based on the EASAs. In the high potential ranges, the order of the specific area ORR activity of the as-prepared electrocatalysts is d-PtIr/C > s-PtIr/C > Pt/C. In particular, the d-PtIr/C exhibited much higher specific area kinetic current density than the s-PtIr/C and Pt/C (Fig. 6e). Also, the specific mass-kinetic current density ($J_{k,Mass}$) of the d-

PtIr/C (58.3 A g^{-1}_{Pt}) at 0.85 V was ~3.43 times higher than that of the Pt/C (17.0 A g-1Pt). Furthermore, Fig. 6a-c shows the ORR measurements before and after the stability test between 0.3 and 1.0 V with a scan rate of 5 mV s^{-1} in O_2-saturated 0.1 M $HClO_4$. In the case of half-wave potentials ($E_{1/2}$), the d-PtIr/C and s-PtIr/C exhibited a slight decrease of ~8 and ~11 mV, respectively, whereas Pt/C exhibited a significant decrease of ~36 mV. The d-PtIr/C and s-PtIr/C showed a slight reduction of size and almost the same morphology after the stability test in Fig. S9, maintaining a much improved electrocatalytic activity. In contrast, after the stability test, the Pt/C exhibited a non-uniform size distribution due to instability of metal electrocatalysts resulting in a deteriorated catalytic activity. As a result, it can be concluded that the d-PtIr/C exhibits much improved electrocatalytic activity and stability for EOR and ORR due to the alloy dendritic nanostructure with high EASA compared to the s-PtIr/C and Pt/C. However, since the composition control in Pt-based alloy nanostructures for the enhanced electrochemical properties is another important factor, the further works will be carried out to confirm the effect of composition in the PtIr alloy dendritic nanostructures on electrocatalytic properties of ethanol oxidation and oxygen reduction reactions.

Conclusions

We prepared the PtIr alloy dendritic NPs as an electrocatalyst for EOR and ORR using a thermal decomposition method in the presence of CTAC. The as-synthesized PtIr NPs exhibited a well-defined alloy structure between Pt and Ir with a dendritic-like shape and over 99% yield. Furthermore, we found remarkably improved electrochemical activity and stability of d-PtIr/C in EOR and ORR; i.e., an improved specific current density, kinetic activity, and electrochemical stability due to a dendritic nanostructure with high EASA, homogeneous alloy bulk and surface composition, and dominant metallic state. Thus, the d-PtIr/C electrocatalyst is expected to be suggested as a promising candidate in both direct ethanol fuel cells and proton exchange membrane fuel cells.

Acknowledgements

This work was supported by the International Collaborative Energy Technology R&D Program of the Korea Institute of Energy Technology Evaluation and Planning (KETEP), granted financial resource from the Ministry of Trade, Industry & Energy, Republic of Korea. (No. 20148520120160).

References

1 Y.-W. Lee, S. N. Cha, K.-W. Park, J. I. Sohn and J. M. Kim, *J. Nanomater.,* 2015, **2015,** 272620.
2 S. Guo, S. Zhang and S. Sun, *Angew. Chem. Int. Ed.,* 2013, **52,** 8526-8544.
3 H. Uchida, N. Ikeda and M. Watanabe, *J. Electroanal. Chem.,* 1995, **391,** 119-123.
4 J.-K. Oh, Y.-W. Lee, S.-B. Han, A-R. Ko, D.-Y. Kim, H.-S. Kim, S.-J. Kim. B. Roh, I. Hwang and K.-W. Park, *Catal. Sci. Technol.,* 2011, **1,** 394-396.
5 K. Kinoshita, *J. Electrochem. Soc.,* 1990, **137,** 845-848.
6 H. Wang, L. Wang, T. Sato, Y. Sakamoto, S. Tominaka, K. Miyasaka, N. Miyamoto, Y. Nemoto, O. Terasaki and Y. Yamauchi, *Chem. Mater.,* 2012, **24,** 1591-1598.
7 H. Ataee-Esfahani, Y. Nemoto, L. Wang and Y. Yamauchi, *Chem. Commun.,* 2011, **47,** 3885-3887.
8 Y. Yamauchi, *J. Ceram. Soc. Jpn.,* 2013, **121,** 831-840.
9 D.-Y. Kim, S.-B. Han, Y.-W. Lee and K.-W. Park, *Mater. Chem. Phys.,* 2013, **137,** 704-708.
10 J. Greeley, I. E. L. Stephens, A. S. Bondarenko, T. P. Johansson, H. A. Hansen, T. F. Jaramillo, J. Rossmeisl, I. Chorken-dorff and J. K. Norskov, *Nat. Chem.,* 2009, **1,** 552-556.
11 D. Y. Chung, Y.-H. Chung, N. Jung, K.-H. Choi and Y.-E. Sung, *Phys. Chem. Chem. Phys.,* 2013, **15,** 13658-13663.
12 V. R. Stamenkovic, B. S. Mun, M. Arenz, K. J. J. Mayrhofer, C. A. Lucas, G. Wang, P. N. Ross and N. M. Markovic, *Nat. Mater.*, 2007, **6,** 241-247.
13 J. Snyder, I. McCue, K. Livi and J. Erlebacher, *J. Am. Chem. Soc.,* 2012, **134,** 8633-8645.
14 Y.-W. Lee, A-R. Ko, S.-B. Han, H.-S. Kim and K.-W. Park, *Phys. Chem. Chem. Phys.,* 2011, **13,** 5569-5572.
15 Y.-W. Lee, A-R. Ko, D.-Y. Kim, S.-B. Han and K.-W. Park, *RSC Adv.,* 2012, **2,** 1119-1125.
16 W. Chen and S. Chen, *J. Mater. Chem.,* 2011, **21,** 9169-9178.
17 J. Kua and W. A. Goddard III, *J. Am. Chem. Soc.,* 1999, **121,** 10928-10941.
18 K. Wang, H. A. Gasteiger, N. M. Markovic and P. N. Ross, *Electrochim. Acta*, 1996, **41,** 2587-2593.
19 X. Teng, S. Maksimuk, S. Frommer and H. Yang, *Chem. Mater.,* 2007, **19,** 36-41.
20 C. Xu, Q. Li, Y. Liu, J. Wang and H. Geng, *Langmuir,* 2012, **28,** 1886-1892.
21 S.-I Choi, R. Choi, S. W. Han and J. T. Park, *Chem. Commun.,* 2010, **46,** 4950-4952.
22 B. Hammer and J. K. Nørskov, *Adv. Catal.,* 2000, **45,** 71-129.
23 T. Gunji, G. Saravanan, T. Tanabe, T. Tsuda, M. Miyauchi, G. Kobayashi, H. Abe and F. Matsumoto, *Catal. Sci. Technol.,* 2014, **4,** 1436-1445.
24 V. Viswanathan, H. A. Hansen, J. Rossmeisl and J. K. Nørskov, *J. Phys. Chem. Lett.,* 2012, **3,** 2948-2951.
25 X. Liu, X. Wu and K. Scott, *Catal. Sci. Technol.,* 2014, **4,** 3891-3898.
26 W. Du, Q. Wang, D. Saxner, N. A. Deskins, D. Su, J. E. Krzanowski, A. I. Frenkel and X. Teng, *J. Am. Chem. Soc.,* 2011, **133,** 15172-15183.
27 W. Du, N. A. Deskins, D. Su and X. Teng, *ACS Catal.,* 2012, **2,** 1226-1231.
28 T. Ioroi and K. Yasuda, *J. Electrochem. Soc.,* 2005, **152,** A1917-A1924.
29 N. Tian, Z.-Y. Zhou, S.-G. Sun, Y. Ding and Z. L. Wang, *Science,* 2007, **316,** 732-735.
30 W. Zhou, J. Wu and H. Yang, *Nano Lett.,* 2013, **13,** 2870-2874.
31 X. Huang, Z. Zhao, J. Fan, Y. Tan and N. Zheng, *J. Am. Chem. Soc.,* 2011, **133,** 4718-4721.
32 L. Wang, H. Wang, Y. Nemoto and Y. Yamauchi, *Chem. Mater.,* 2010, **22,** 2835-2841.
33 A. R. Tao, S. Habas and P. Yang, *Small,* 2008, **4,** 310-325.
34 B. Lim and Y. Xia, *Angew. Chem. Int. Ed.,* 2011, **50,** 76-85.
35 X. Yu, Y. Zhang, L. Guo and L. Wang, *Nanoscale,* 2014, **6,** 4806-4811.
36 F. Jia, F. Wang, Y. Lin and L. Zhang, *Chem. Eur. J.,* 2011, **17,** 14603-14610.
37 Y.-W. Lee, B.-Y. Kim, K.-H. Lee, W.-J. Song, G. Cao and K.-W. Park, *Int. J. Electrochem. Sci.,* 2013, **8,** 2305-2312.

38 J. K. Kawasaki and C. B. Arnold, *Nano Lett.,* 2011, **11,** 781-785.
39 J. Y. Cheon, T. Kim, Y.M. Choi, H. Y. Jeong, M. G. Kim, Y. J. Sa, J. Kim, Z. Lee, T.-H. Yang, K. Kwon, O. Terasaki, G.-G. Park, R. R. Adzic and S. H. Joo, *Sci. Rep.,* 2013, **3,** 2715.
40 40 A. Kong, X. Zhu, Z. Han, Y. Yu, Y. Zhang, B. Dong and Y. Shan, *ACS Catal.,* 2014, **4,** 1793-1800.
41 Y.-W. Lee, S.-B. Han, D.-Y. Kim and K.-W. Park, *Chem. Commun.,* 2011, **47,** 6296-6298.
42 J.-N. Zheng, L.-L. He, F.-Y. Chen, A.-J. Wang, M.-W. Xue and J.-J. Feng, *J. Mater. Chem. A,* 2014, **2,** 12899-12906.
43 L.-X. Ding, A.-L. Wang, G.-R. Li, Z.-Q. Liu, W.-X. Zhao, C.-Y. Su and Y.-X. Tong, *J. Am. Chem. Soc.,* 2012, **134,** 5730-5733.
44 C. Alegre, D. Sebastián, M. E. Gálvez, R. Moliner, A. Stassi, A. S. aricò, M. J. Lázaro and V. Baglio, *Catalysts,* 2013, **3,** 744-756.
45 D. R. M. Godoi, J. Perez and H. M. Villullas, *J. Power Sources,* 2010, **195,** 3394-3401.
46 S. J. Hwang, S. J. Yoo, T.-Y. Jeon, K.-S. Lee, T.-H. Lim, Y.-E. Sung and S.-K. Kim, *Chem. Commun.,* 2010, **46,** 8401-8403.
47 R. Manoharan and J. B. Goodenough, *J. Mater. Chem.,* 1992, **2,** 875-887.
48 Z. Liu, X. Y. Ling, X. Su, J. Y. Lee and L. M. Gan, *J. Power Sources,* 2005, **149,** 1-7.

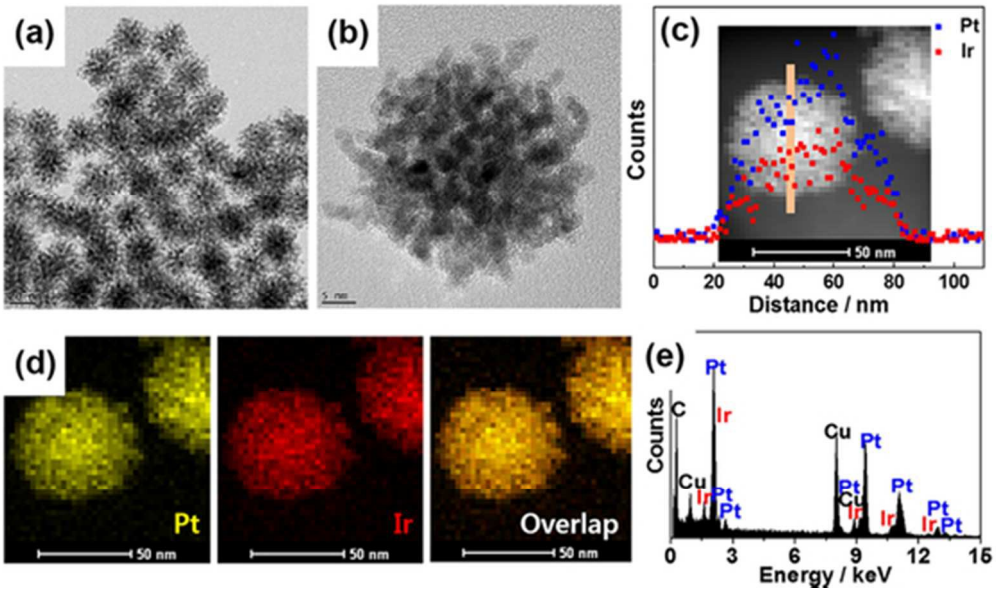

(a) FE-TEM and (b) HR-TEM images of the PtIr alloy dendritic nanostructures. (c) Line-scanning profile across the PtIr alloy dendritic nanostructures. [The inset indicates the HAADF-STEM image of the PtIr alloy nanostructures for line-scanning profiles] (d) HAADF-STEM image of the PtIr alloy nanostructures and STEM-EDX element maps for the Pt and Ir. (e) EDX spectrum of the PtIr alloy dendritic nanostructures.
47x27mm (300 x 300 DPI)

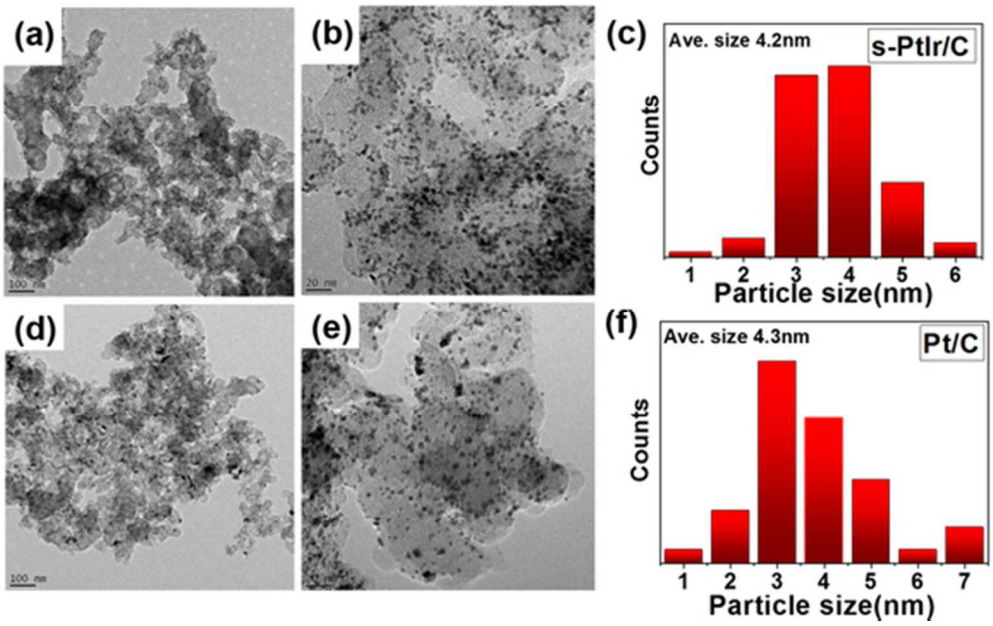

(a and b) FE-TEM images of the s-PtIr NPs deposited on carbon black. (c) Particle size distribution of s-PtIr NPs. (d and e) FE-TEM images of the Pt NPs deposited on carbon black (E-TEK, Co.). (f) Particle size distribution of the Pt/C NPs.
49x30mm (300 x 300 DPI)

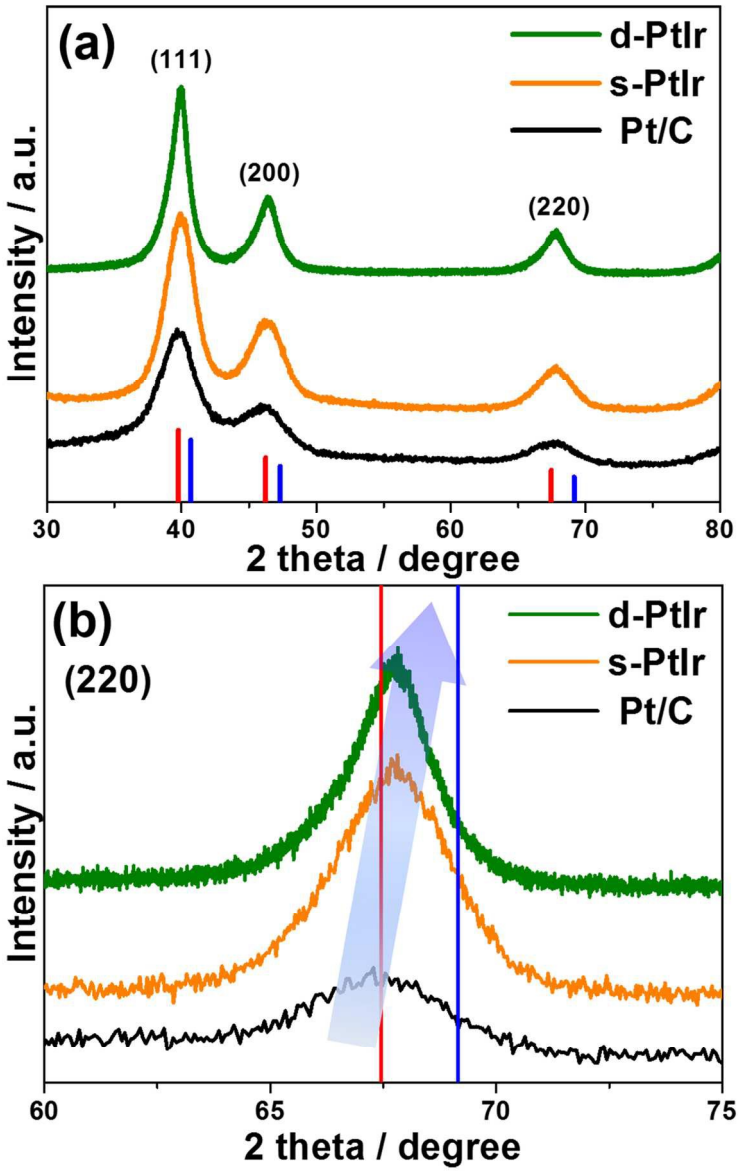

(a) Wide-range XRD patterns of the d-PtIr/C, s-PtIr/C, and Pt/C in comparison with XRD reference data of Pt (red) and Ir (blue). (b) The diffraction peaks of (220) planes in the electrocatalysts are compared with XRD reference data of Pt (JCPDS No. 04-0802) and Ir (JCPDS No. 87-0715).
123x190mm (300 x 300 DPI)

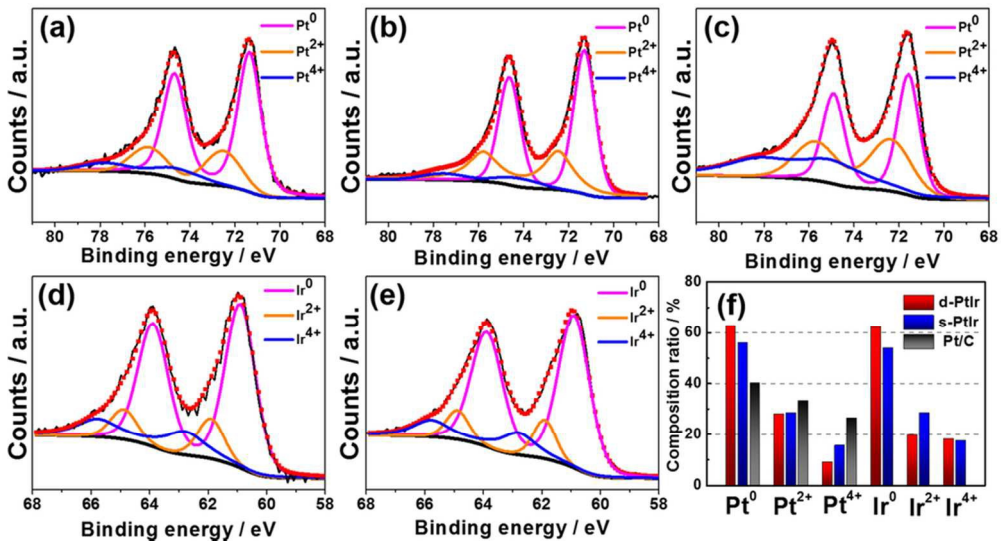

Surface and chemical analysis using XPS. Pt 4f spectra in (a) d-PtIr/C, (b) s-PtIr/C, and (c) Pt/C. Ir 4f spectra in (d) d-PtIr/C and (e) s-PtIr/C. (f) Comparison of chemical states and ratios of Pt 4f and Ir 4f spectra of the as-prepared NPs measured and calculated from the XPS fitting data.
86x46mm (300 x 300 DPI)

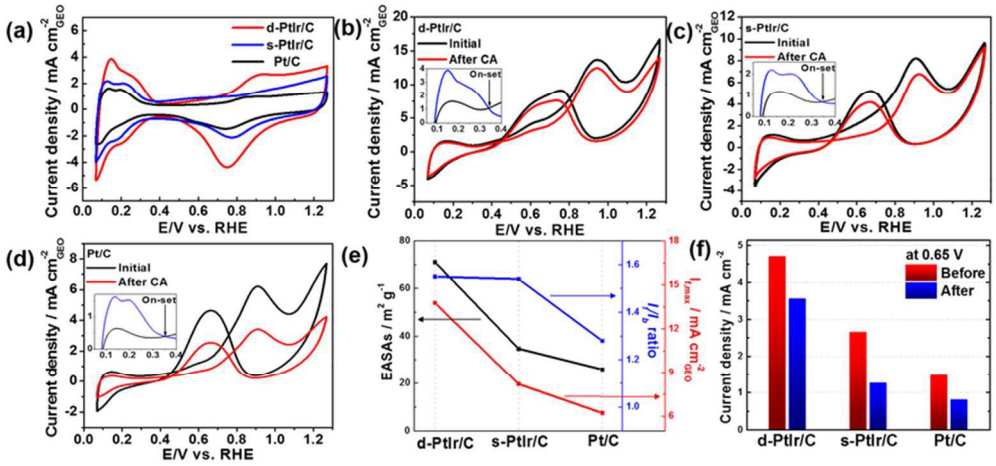

(a) CVs of the d-PtIr/C s-PtIr/C, and Pt/C in Ar-saturated 0.1 M HClO4 with a scan rate of 50 mV·s-1 at 25 oC. CVs before and after the stability test of the (a) d-PtIr/C, (b) s-PtIr/C, and (c) Pt/C electrocatalysts in 0.1 M HClO4 + 0.2 M C2H5OH. The insets indicate CVs in 0.1 M HClO4 (blue line) and 0.1 M HClO4 + 0.2 M C2H5OH (black line) of the as-prepared electrocatalysts. (e) Comparison of EASAs, If/Ib, and maximum current density of forward scan (If,max) of the d-PtIr/C s-PtIr/C, and Pt/C with a scan rate of 50 mV·s-1 at 25 oC. (f) Comparison of current density of the as-prepared electrocatalysts before and after stability test at 0.65 V.
75x35mm (300 x 300 DPI)

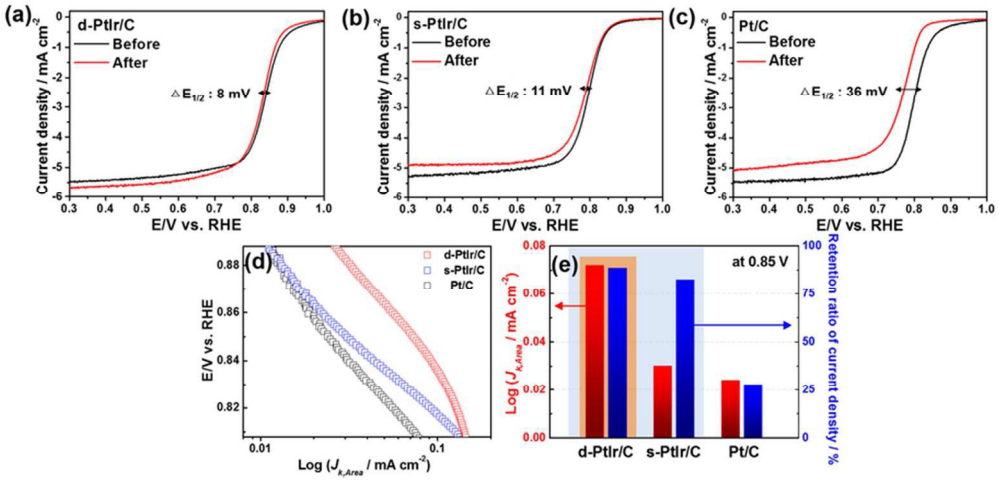

Comparison of ORR polarization curves of (a) d-PtIr/C, (b) s-PtIr/C, and (c) Pt/C electrocatalysts before and after stability test in O2–saturated 0.1 M HClO4 with a scan rate of 5 mV·s-1. (d) Specific area-kinetic activity curves of as-prepared electrocatalysts in ORR normalized to the EASAs. (e) Specific area-kinetic current density and retention ratio of current density of the as-prepared electrocatalysts measured at 0.85 V before and after stability test.
77x37mm (300 x 300 DPI)

A table of contents entry

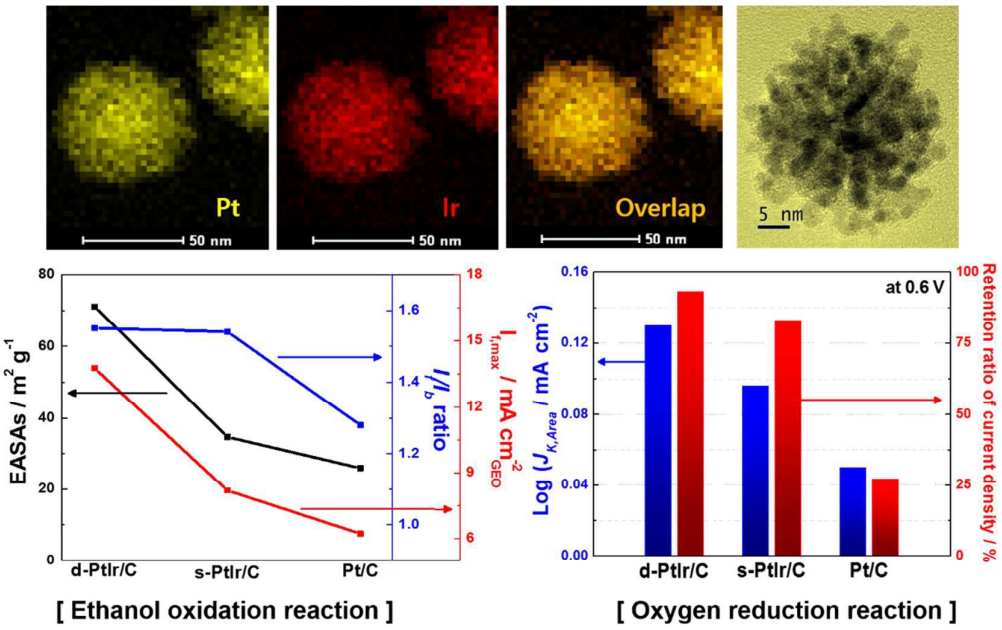

The PtIr alloy dendritic nanostructures with high surface area exhibit superior electrocatalytic properties in ethanol oxidation and oxygen reduction reactions.